Physics of Fluids

RESEARCH ARTICLE | DECEMBER 05 2023

Pinch-off dynamics in unequal-size droplets head-on collision on a wetting surface: Experiments and direct numerical simulations ⊘

Saroj Ray ⓘ ; Yu Han (韩禹) ⓘ ; Song Cheng (成松) ✉ ⓘ

[Check for updates]

View Online   Export Citation

Articles You May Be Interested In

Head-on collision of unequal-size droplets on a wetting surface

Physics of Fluids (February 2023)

Coalescence dynamics of unequal sized drops

Physics of Fluids (January 2019)

Numerical investigations of head-on collisions of binary unequal-sized droplets on superhydrophobic walls

Physics of Fluids (March 2021)

Pinch-off dynamics in unequal-size droplets head-on collision on a wetting surface: Experiments and direct numerical simulations

View Online   Export Citation   CrossMark

Saroj Ray,[1] (iD) Yu Han (韩禹),[1] (iD) and Song Cheng (成松)[1,2,a] (iD)

AFFILIATIONS

[1]Department of Mechanical Engineering, The Hong Kong Polytechnic University, Hung Hom, Kowloon, Hong Kong
[2]Research Centre for Resources Engineering towards Carbon Neutrality, The Hong Kong Polytechnic University, Hung Hom, Kowloon, Hong Kong

[a]Author to whom correspondence should be addressed: songryan.cheng@polyu.edu.hk

ABSTRACT

There is a growing interest in the optimization of spray systems to minimize reflexive separation and enhance droplet coalescence, which has the potential to greatly benefit industrial and agricultural applications. In this investigation, the pinch-off dynamics in head-on impacts of unequal-size droplets on a hydrophobic surface are explored, employing both experimental and numerical approaches. The study focuses on size ratios ranging from 1.0 to 5.0 and impact Weber numbers up to 208. The captured images from the high-speed camera are meticulously processed and analyzed in a detailed manner. Two distinct scenarios are observed in the experimental findings: (1) reflexive separation occurring without the formation of satellite droplets and (2) reflexive separation characterized by the presence of satellite droplets. Direct numerical simulations are also conducted to probe the underlying dynamics during droplet impact. The direct numerical simulation results closely replicate the experimental results, demonstrating excellent agreement with the dynamics of the pinch-off process. The simulated velocity field demonstrates the liquid's movement away from the neck region, leading to progressive thinning and eventual pinch-off. Furthermore, the study examines the evolution of the neck radius over time (τ), revealing a linear variation in log–log plots. Remarkably, the neck radius scales with $\tau^{2/3}$, even for different size ratios. A regime diagram in We–Δ space is reported.

I. INTRODUCTION

Understanding the mechanics of reflexive separation (RS) during droplet-on-droplet impacts, particularly when a moving droplet collides with another droplet on a solid surface, is essential for several practical applications including industrial spray coating, agricultural spraying, and combustion systems. A prominent example is spray coating in industrial, where the quality of the coating depends on the size and velocity of the droplets and their ability to coalesce with each other and with the substrate. Reflexive separation can lead to uneven coatings and wasted material, which can be costly and time-consuming. By understanding the conditions that lead to reflexive separation, the spray system can be optimized to produce a more uniform and efficient coating.[1,2] In agricultural spraying, reflexive separation can affect the efficacy of pesticides and fertilizers. Uneven droplet distribution can lead to areas of over- or under-treatment, which can have negative environmental and economic impacts. Better understanding and controlling droplet behavior can aid to optimize spray to maximize crop yield and minimize waste.[3,4] In combustion systems, uneven droplet distribution can lead to areas of fuel–rich or fuel–lean mixtures, which can reduce combustion efficiency and increase emissions.[5]

Previous research has extensively studied the collision of two droplets, particularly for water at atmospheric pressure. The majority of previous studies[6–9] have primarily focused on identifying and interpreting different outcomes that arise from droplet collisions. These outcomes include coalescence, bouncing, reflexive separation, and splattering or shattering.[10,11] These investigations have led to the development of a well-established collision nomogram in the We–B parameter space, which demonstrated that the collision outcomes mainly affect the impact Weber number (We) and the impact parameter (B).[9] For two droplets colliding with relative velocity U, radius R, density ρ, and surface tension γ, the impact Weber number is defined as $We = 2\rho U^2 R/\gamma$ which measures the relative significance of droplet inertia compared to the surface tension. The impact parameter (B) measures the deviation of the colliding trajectory from an exact

head-on collision, with $B = 0$ representing head-on collision and $B = 1$ gazing collision. Studies have observed that droplet bouncing occurs at low Weber numbers, while separation with satellite droplet formation occurs at moderately higher Weber numbers. Furthermore, the collision outcomes influence several other factors such as Ohnesorge number, defined as $Oh = \mu/(\rho R \gamma)^{1/2}$, where μ represents the dynamic viscosity of the liquid.[11–14] The Ohnesorge number quantifies the relative contributions of liquid viscosity and capillary pressure. Water and hydrocarbon have quite different Oh number (due to different viscosity and surface tension) and thus show different collision behaviors.[11] It has been found that the size ratio (Δ, defined as the ratio of the big droplet radius to small droplet radius), which characterizes the discrepancy in droplet sizes, is a crucial factor that affects collision outcomes.[6,15] Recent studies have examined the dynamics of head-on collisions between droplets with varying sizes, as well as the occurrence of satellite droplets during the partial coalescence of unequal-sized droplets made up of the same liquid. The formation of satellite droplets and pinch-off dynamics during the partial coalescence of droplets with varying sizes but composed of the same liquid were numerically studied by Deka et al.[16] Their results revealed a positive correlation between the critical diameter ratio for satellite formation and the viscosity of both the droplet and surrounding fluids. Chaitanya et al.[17] studied the dynamics of oblique collision between unequal-sized liquid droplets and found that the collision outcomes were influenced by the asymmetric flow caused by the droplets' different sizes and the oblique collision. Another factor affecting the collision outcomes is the gas environment. It has been observed that higher gas pressures favor droplet bouncing and lower gas pressures promote droplet coalescence.[7,18]

Studies on droplet impact onto a pool of same liquid have also been carried out, due to the experimental simplicity and the retention of key physics applicable to related practical scenarios. When a droplet is gently placed onto a pool same liquid, it has been observed that the coalescing droplet can pinch off and produce a smaller droplet (referred to as a satellite droplet). Thoroddsen and Takehara[19] experimentally observed that the satellite droplets can undergo coalescence once again. They found that the coalescence process occurs in a cascade sequence, whereby each subsequent step generates a drop of reduced size. However, the cascade will not continue indefinitely due to the impact of viscous effects. Blanchette and Bigioni[20] corroborated that, in more viscous fluids, the capillary wave is suppressed, and as a result, the droplet is not stretched enough to break apart into smaller droplets. Instead, the droplet merges with the liquid pool. They also determined the maximum Oh number below which partial coalescence occurs is 0.026 at low Bond numbers ($Bo = \rho g R_f^2/\gamma$, where g is acceleration due to gravity) which indicate negligible gravitational effect.

At low Weber number [$We = O(1)$], binary collision of unequal-size droplets can cause partial coalesce. Zhang et al.[21] experimentally investigated the formation of satellite droplets during the coalescence of two droplets of unequal-size in air at low impact Weber number [$We = O(1)$]. They found that the critical value of size ratio Δ above which satellite formation occurs is 1.55 at low Oh number, and the critical size ratio increases monotonically with increasing Oh number.

At high impact Weber number [i.e., $O(100)$], head-on droplet collisions result in an interesting collision outcome known as reflexive separation (RS) which have been studied less extensively. Initially, during the collision, the droplets merge. However, shortly after the coalescence, the droplets abruptly separate from each other. This separation is caused by

the release of surface tension energy accumulated during the coalescence process. It has been revealed that the occurrence of separation in droplet collisions and the number of satellite droplets generated are influenced by the viscosity of the liquid and the size of the droplets.[15,22] A liquid ligament is formed during the separation process, and the breakup of this ligament into smaller droplets can be attributed to the Plateau–Rayleigh instability (P–R instability).[15,23] Huang et al.[24] studied the reflexive separation in head-on collision of two droplets. They found that collisions between unequal-sized droplets with asymmetric impacts can suppress the formation of satellite droplets. Deka et al.[25] numerically studied the head-on collision of equal-size droplets with different viscosities. They demonstrate that differences in viscosity between colliding drops can result in two additional outcomes: encapsulation and crossing separation. However, these studies did not focus on droplets pinch-off during droplet collisions with a solid surface.

In recent years, several studies have focused on exploring the dynamics of a falling droplet as it impacts a sessile droplet, yielding valuable insights into the interaction between droplets on solid surfaces. The collision outcomes of falling droplet with sessile droplet on hydrophilic,[26] hydrophobic,[27] and superhydrophobic[28] surfaces have been investigated. It has been found that coalescence, bouncing, and complete rebounding of droplets can occur depending on the behavior of solid surfaces (i.e., wettability). Ramírez-Soto et al.[29] utilized both experiments and direct numerical simulations (DNS) to explore the collision dynamics of an oil droplet impacting a sessile droplet on a superamphiphobic surface. Kumar et al.[30] conducted an experimental study focusing on the coalescence dynamics of drop-on-drop impact involving ethanol droplets on a hydrophilic surface. They characterized the coalescence process into two categories: complete coalescence and partial coalescence. In the case of partial coalescence, the merged droplets underwent a pinching-off process, resulting in the formation of a smaller daughter droplet. Furthermore, Abouelsoud and Bai[31] investigated the impact outcomes in relation to wettability by employing various solid surfaces such as smooth glass, aluminum, copper, Teflon, and coated glass. They observed complete coalescence for droplet impacts on hydrophobic surfaces, such as coated glass with a contact angle of 119°. Meanwhile, both coalescence and bouncing were observed for hydrophilic surfaces, with the specific outcome depending on the Weber number. In a recent study, Ray et al.[32] conducted an experimental study to investigate the collision dynamics of droplets with different sizes on a wetting surface, specifically focusing on large size ratios [$\Delta = O(10)$]. They observed various collision outcomes, including droplet coalescence, bouncing, and partial coalescence.

Recently, the collisions of a spinning droplet with a non-spinning droplet have been investigated by He and Zhang.[33] They found that for head-on collision of equally-sized droplets of the same liquid, the spinning droplet can generate significant non-axisymmetric flow patterns. Furthermore, He et al.[34] studied self-spin in a non-spinning droplet through its oblique impact on a non-slip boundary and corroborated that higher impact velocity or increased liquid viscosity leads to a higher angular speed of the spinning droplet.

Numerous studies have explored the impact of droplets onto a pool of fluid, as it captures the majority of physics relevant to related applications. Kirar et al.[35] studied the coalescence dynamics of two droplets impacting pool of the same liquid. They demonstrated that for large normalized distance between the impacting droplets (i.e., >3.2), the capillary waves of the droplets do not interact. A new quasi-potential

model was developed by Alventosa et al.[36] to examine the bouncing phenomenon of a droplet on a liquid pool in the inertio-capillary regime. There has also been significant interest in the phenomenon of droplets repeatedly bouncing on a vertically oscillated liquid pool.[37,38]

The aforementioned studies primarily investigate either binary droplet collisions across a wide range of *We* numbers without the involvement of a solid surface or the impact of a falling droplet onto a sessile droplet with *We* number below 50. Therefore, in this paper, we experimentally and numerically study the pinch-off dynamics in head-on collision of unequal-size droplets on a hydrophobic surface at the impact *We* number up to 208, which remains unexplored. By delving into these collision dynamics and studying the pinch-off phenomenon, this study aims to contribute to a deeper understanding of droplet interactions on hydrophobic surfaces under high *We* number conditions. The collision outcomes examined in this study are depicted within the blue dotted box in Fig. 1 to showcase the contrast in collision results investigated in earlier studies.

The rest of the article is organized in the following manner. In Sec. II, the experimental procedure and numerical method used in the study are presented. The experimental and numerical results, along with their comparisons, are thoroughly explored and discussed in Sec. III. Finally, Sec. IV presents a summary of the important findings from this study.

II. METHODOLOGY

A. Experiment

The hydrophobic surface used in this study is prepared by coating polyvinyl chloride (PVC) with neverWet multi-surface spray. The
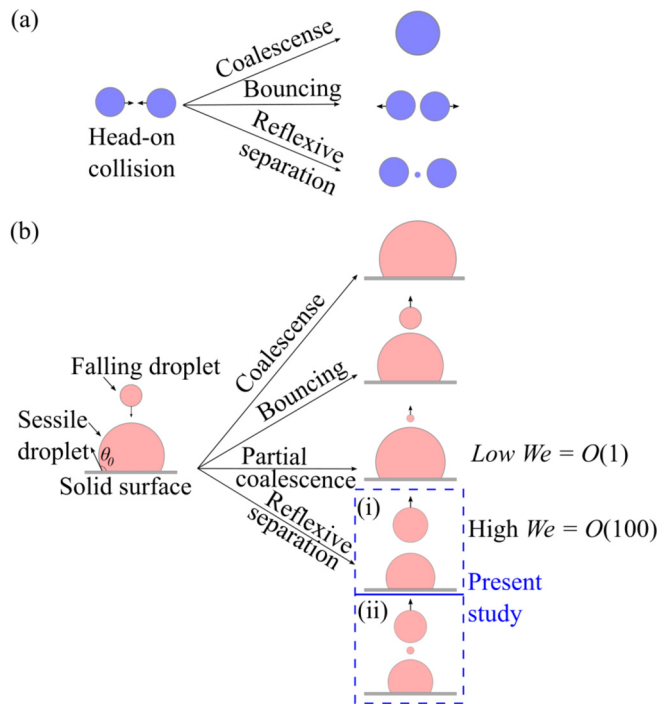

FIG. 1. A pictorial depiction of the different outcome during the head-on collision of (a) two droplets, and (b) a falling droplet with a sessile droplet on a solid surface.

liquid employed in the experiments was distilled water, and experiments were performed at room temperature (25 °C). To obtain time-resolved images, the collision process is recorded using two high-speed cameras. The main camera used is a Photron SZ-A high-speed camera, mounted with a Questar QM-100 lens, set to capture at 40 000 fps with a spatial resolution of 1024×512. In order to achieve accurate droplet impact alignment, a second camera, the Chronos 2.1 from Kron Technologies Inc., is positioned normal to the plane of the previous camera and droplet motion. This camera is equipped with a TCLO lens and is set to record at a high frame rate of 7135 fps, capturing images with a spatial resolution of 640×360. Backlit lighting is provided by two lights. Post-processing of the recorded videos is carried out using a combination of photron FASTCAM viewer (PFV) and custom scripts developed in-house. More detailed description of the experimental apparatus used in this study can be found in our previous study.[32] Table I provides a summary of the experimental conditions employed in the study.

B. Numerical method

The fluid flow being analyzed is assumed to be incompressible, and the fluids are considered to be Newtonian. The equations that describe the fluid flow are the continuity equation and the Navier–Stokes equations and are expressed as

$$\nabla \cdot \mathbf{u} = 0, \tag{1}$$

$$\rho \left[\frac{\partial \mathbf{u}}{\partial t} + \mathbf{u} \cdot \nabla \mathbf{u} \right] = -\nabla p + \nabla \cdot (2\mu \mathbf{D}) + \gamma \kappa \mathbf{n} \delta_s, \tag{2}$$

where $\mathbf{u}$, ρ, p, and μ represent the velocity vector, the density, the pressure, and the dynamic viscosity, respectively, and $\mathbf{D}$ is the deformation tensor defined as $(\nabla \mathbf{u} + \nabla \mathbf{u}^T)/2$. The surface tension term in Eq. (2), represented by the last term on the right-hand side, is modeled using the continuum-surface-force (CSF) model developed by Brackbill et al.[39] Here, δ_s, γ, κ, and $\mathbf{n}$ are the Dirac delta function, surface tension coefficient, local curvature, and the unit vector. Equations (1) and (2) are solved using the standard fractional-step projection method.

The advection equation governs the volume fractions c used to track the interface of droplet in the employed conventional geometric volume-of-fluid (VOF) method with height function curvature estimation. To accurately capture the interface, an adaptive mesh refinement

TABLE I. Experimental conditions and parameter values studied in this work.

Parameter	This study	
	Case E1	Case E2
Falling droplet diameter (mm)	0.456	0.488
Sessile droplet diameter (mm)	1.368	1.220
Static contact angle, θ_0, (deg)	128	105
Size ratio, $\Delta = R_s/R_f$	3.0	2.5
Weber number, $We = 2\rho_l U_0^2 R_f/\gamma$	208	168
Ohnesorge number, $Oh = \mu_l/(\rho_l R_f \gamma)^{1/2}$	7.8×10^{-3}	7.5×10^{-3}
Bond number, $Bo = \rho_l g R_f^2/\gamma$	7.0×10^{-3}	8.0×10^{-3}
Reynolds number, $Re = \rho_l U_0 R_f/\mu_l$	1308	1222

(AMR) technique is employed. The advection equation describes the transport of volume fraction c and is expressed as

$$\frac{\partial c}{\partial t} + \nabla \cdot (c\mathbf{u}) = 0. \tag{3}$$

The volume fractions c in the advection equation represent distinct phases, $c = 0$ for the gas phase, $c = 1$ for the liquid phase, and $0 < c < 1$ for the gas–liquid interface. The density and dynamic viscosity are calculated based on these volume fractions. The density of the mixture is determined using the equation $\rho = c \times \rho_l + (1 - c) \times \rho_g$, where ρ_l and ρ_g represent the densities of the liquid and gas phases, respectively. Similarly, the dynamic viscosity is calculated using the equation $\mu = c \times \mu_l + (1 - c) \times \mu_g$, where μ_l and μ_g represent the dynamic viscosities of the liquid and gas phases, respectively. In the simulations, the length is non-dimensionalized using the initial falling droplet radius as the reference length. Additionally, time is non-dimensionalized using the inertial-capillary timescale, denoted as t_c. The inertial-capillary timescale is defined as the square root of $(\rho_l R_f^3/\gamma)$, where R_f denotes the radius of the falling droplet and γ represents the surface tension.

Simulations provide insights into energy exchange during collision processes. Energy loss is quantified by the total viscous dissipation (ϵ_η), which can be obtained by integrating the total dissipation rate (ϕ) across the entire control volume, and expressed as

$$\phi = 2\mu \left[\left(\frac{\partial u_1}{\partial x} \right)^2 + \left(\frac{\partial u_2}{\partial y} \right)^2 + \left(\frac{\partial u_3}{\partial z} \right)^2 \right]$$
$$+ \mu \left[\left(\frac{\partial u_1}{\partial y} + \frac{\partial u_2}{\partial x} \right)^2 + \left(\frac{\partial u_2}{\partial z} + \frac{\partial u_3}{\partial y} \right)^2 + \left(\frac{\partial u_3}{\partial x} + \frac{\partial u_1}{\partial z} \right)^2 \right], \tag{4}$$

where u_1, u_2, and u_3 correspond to the velocity in the x, y, and z coordinate directions, respectively.

The numerical simulations of droplet collisions on a hydrophobic surface are carried out using the open-source software Basilisk C, developed by Popinet.[40] Balilisk C has proven to be proficient in solving diverse multiphase flow problems.[29,36,41,42] Figure 2 illustrates the computational domain used in the simulations, which is axisymmetric with the axis of symmetry located at $r = 0$. At the solid surface positioned at $z = 0$, various boundary conditions are applied, including no-slip, non-penetrable, and zero pressure gradient. Open boundary conditions are employed at the top and side boundaries, while symmetric boundary conditions are used at $r = 0$. The contact angle is specified using the height-function method, which was developed by Afkhami and Bussmann.[43] The values of contact angle used in the simulation are obtained from the experimental images. To ensure a sufficient domain size that minimizes boundary effects, the length and height of the domain are both set to 20 times the falling droplet radius ($L = H = 20R_f$). The computational domain is discretized, with the finest grid points corresponding to 2^{12} uniform grids in each direction. Thus, the minimum cell size is 0.005 times the initial falling droplet radius, which corresponds to a dimensional length of 2 μm with 200 grid points inside the droplets in each direction. In the simulations, CFL (Courant–Friedrichs–Lewy) number equal to 0.5 is used to specify the time steps. Each simulation requires approximately 100 h of physical time to complete on a 3.2 GHz processor with 64 GB of memory.
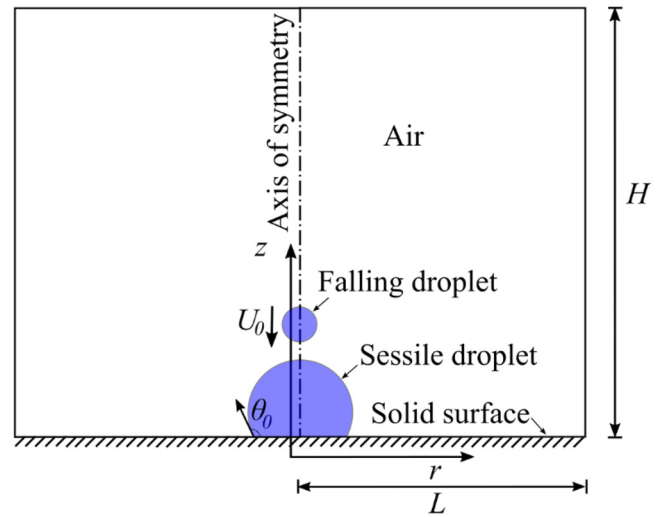

FIG. 2. Schematic illustration of the computational domain. Here, U_0 denotes impact velocity of the falling droplet and θ_0 indicates equilibrium (static) contact angle.

III. RESULTS AND DISCUSSION

A. Experimental observations

To gain a better understanding of satellite droplet formation for unequal-size droplet collision on wetting surface, sequential images of the high-speed camera are processed and analyzed. Figure 3 (Multimedia view) displays snapshots of the reflexive separation (RS) process of a falling droplet and a sessile droplet on a coated PVC surface at $\Delta = 3.0$ (Δ, defined as the ratio of the sessile droplet radius to the falling droplet radius. Note that spherical cap radius of the sessile droplets has been used to define Δ.) and $We = 208$ ($We = 2\rho_l U_0^2 R_f/\gamma$) (corresponding to case E1 in Table I). The equilibrium contact angle (θ_0) is 128°, and the contact angle hysteresis (CAH, defined as the difference of advancing contact angle and the receding contact angle) is 85° which is determined from the experiments. As the impact We number is moderately high, impact of the falling droplet creates a crater at the impact location ($t = 0.10$ ms). This crater depth grows with increasing time, and a rim is seen near the tip of the crater ($t = 0.50$ ms). At t $= 1.00$ ms, the merged droplet exhibits radial expansion, reaching its maximum spreading diameter. Here onward, the merged droplets retract radially inward. The vertical height of the merged droplet is increased, and a liquid-column-like structure is formed at $t = 3.50$ ms. A primary neck is established around the midpoint of the liquid column at t $= 5.00$ ms. Subsequently, the neck shrinks radially with time and eventually breakup at $t = 6.00$ ms. The upper-separated (also large) droplet keeps moving upward as it contains sufficient kinetic energy. The lower-separated droplet retracts downward and stays on the coated PVC as a sessile droplet, although it has a smaller size than the initial sessile droplet size.

Figure 4 (Multimedia view) depicts the snapshots of RS process at $\Delta = 2.5$ and $We = 168$ (corresponding to case E2 in Table I). The collision sequence in this case closely resembles the previous scenario (Fig. 3) until $t = 3.50$ ms (Fig. 4). As the necking of the coalesced
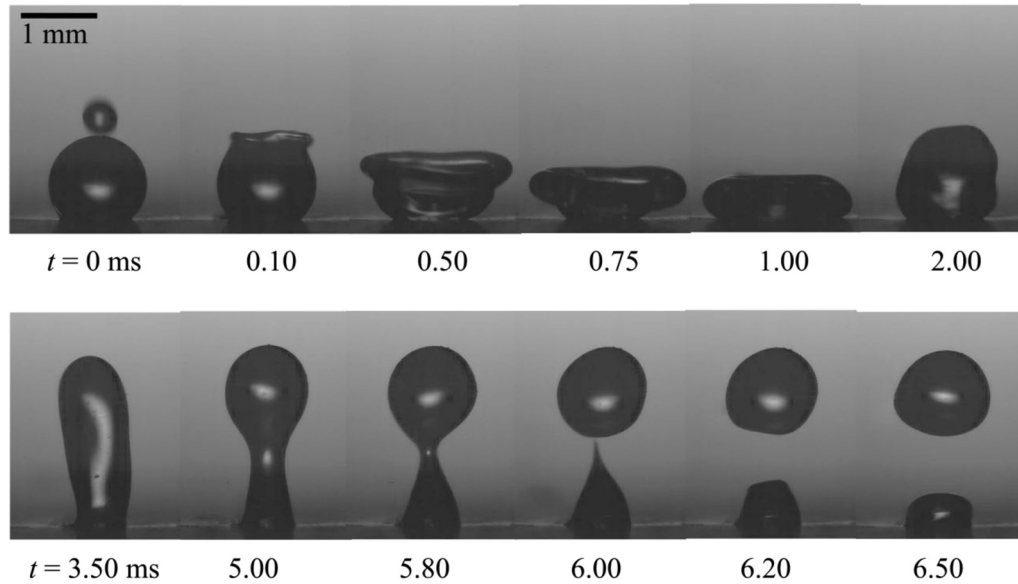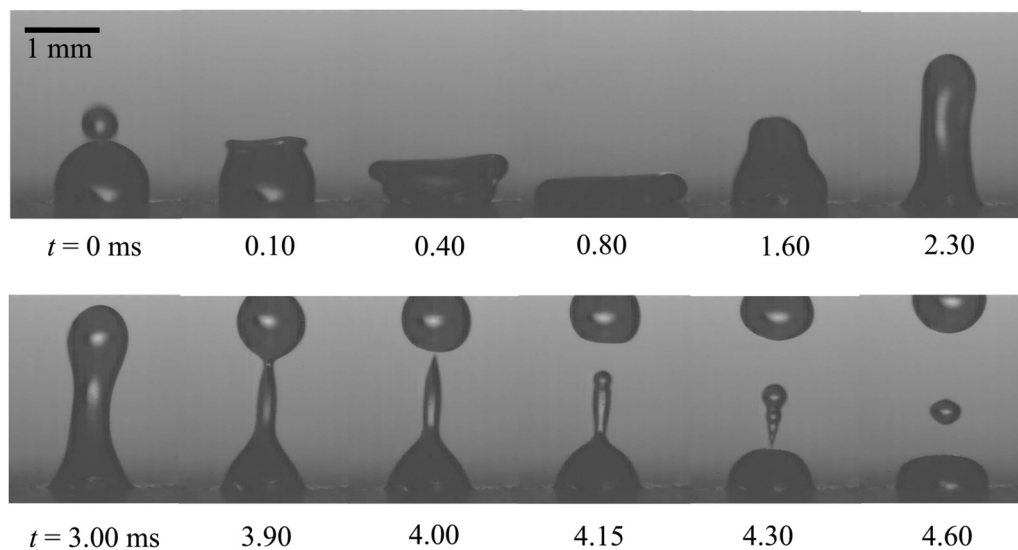
FIG. 3. Photographic images showing the reflexive separation (RS) process of unequal-size droplets on a hydrophobic surface, with no satellite droplets formed ($\Delta = 3.0$, $We = 208$, $\theta_0 = 128°$, CAH $= 85°$). Multimedia available online.

droplet continues to occur, a narrow and long liquid column is formed at $t = 3.90$ ms near the center with spherical and conical liquid region at the top and bottom, respectively. The narrow liquid column pinches off at the top, and a droplet is detached from the rest of the merged liquid mass ($t = 4.00$ ms). The narrow liquid column retracts downward, and capillary wave can be seen to grown on its surface. The bottom end of the narrow liquid column also pinches off at $t = 4.30$ ms and subsequently forms a tiny satellite droplets ($t = 4.60$ ms).

B. Direct numerical simulations

Despite the experimental observations indicating the significance of Δ and We numbers in determining the impact outcomes, detailed information about the velocity fields and energy transfer mechanisms between the droplets is lacking. By conducting DNS simulations and comparing them with experimental data, this information can be determined. Simulations are conducted by solving the dimensionless form of the governing equations, where the length scale and time are

FIG. 4. Photographic images showing the reflexive separation (RS) of unequal-size droplets on a hydrophobic surface with a satellite droplet formed ($\Delta = 2.5$, $We = 168$, $\theta_0 = 105°$, CAH $= 88°$). Multimedia available online.

scaled by the falling droplet radius (R_f) and capillary timescale [$(\rho_l R_f^3/\gamma)^{1/2}$], respectively. This scaling results in the velocity field being scaled by the capillary velocity [$V_\gamma = R_f/t_c = (\gamma/\rho_l R_f)^{1/2}$]. Then, the dimensionless impact velocity is given by $U_0/V_\gamma = (We/2)^{1/2}$.

Figure 5 shows the contour of velocity magnitude, velocity field, pressure, and the rate at which viscous dissipation occurs at $\Delta = 3.0$ and $We = 208$. The simulation results presented in Fig. 5 correspond well with the snapshots of the pinch-off dynamics shown in Fig. 3. By utilizing these vector fields in conjunction with an energy budget analysis, it is possible to quantitatively explore the dynamics of the collision process between droplets on a solid surface. The impact of the falling droplet initiates a flow inside the sessile droplet as it descends. At

$t/t_c = 0.2$, the falling droplet has merged with the sessile droplet, and a thin rim of liquid is formed due to high impact energy of the falling droplet. As the liquid near the impact location is pushed away, a crater is formed, as seen at $t/t_c = 1.2$, and flow is radially outward which further stretches the coalesced droplet radially. At $t/t_c = 2.6$, the flow inside the merged droplet is irregular (complex) due to large surface oscillation, whereas at $t/t_c = 6.0$, the velocity at the tip of the merged droplet is upward and the merged droplet height starts to increase. At $t/t_c = 10.0$, a vortex flow can be seen near the tip region of the merged droplet, whereas middle and lower regions move vertically upward and toward the solid surface, respectively. At $t/t_c = 14.3$, a neck emerges in the middle of the liquid column. Eventually, the merged
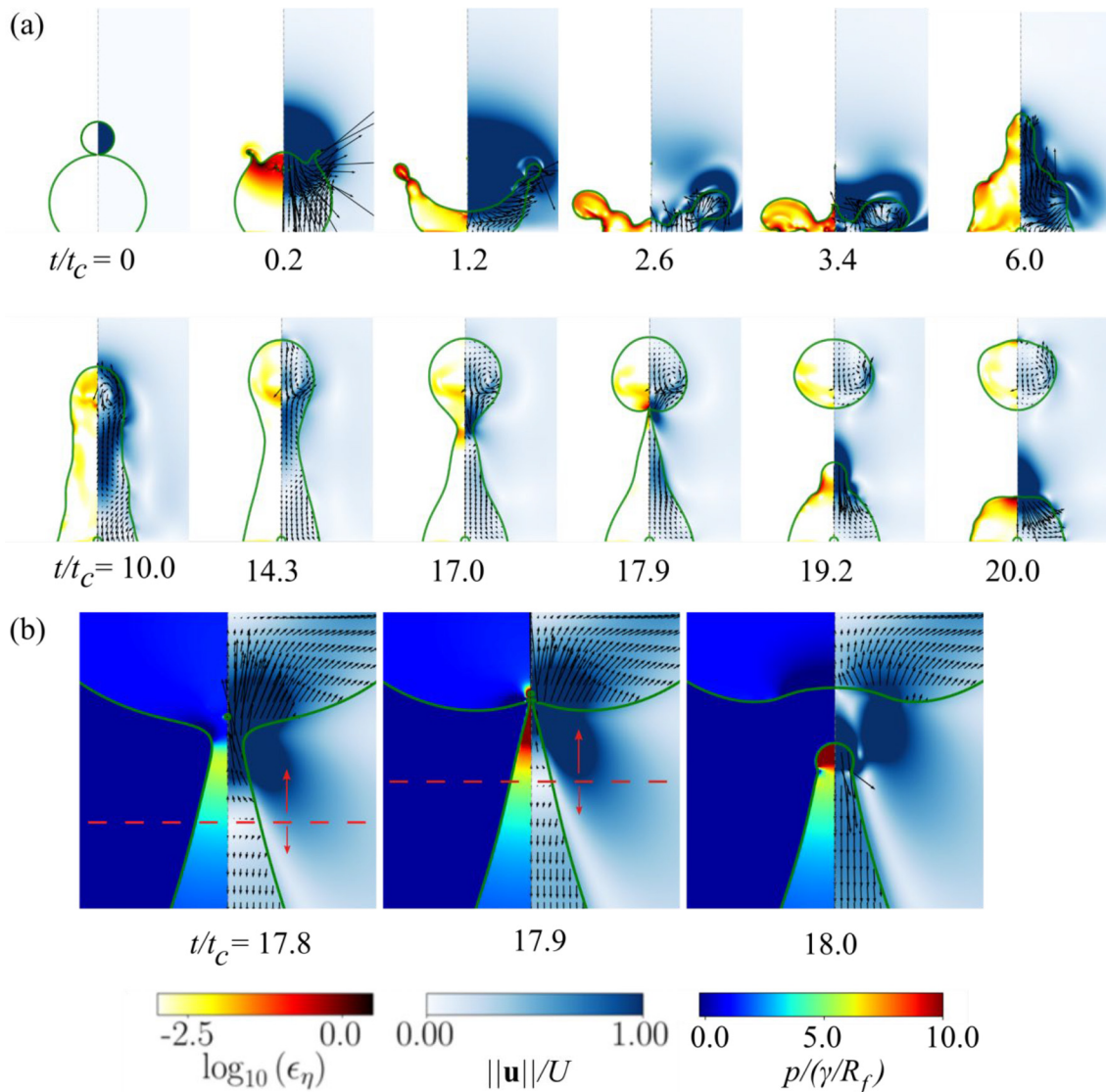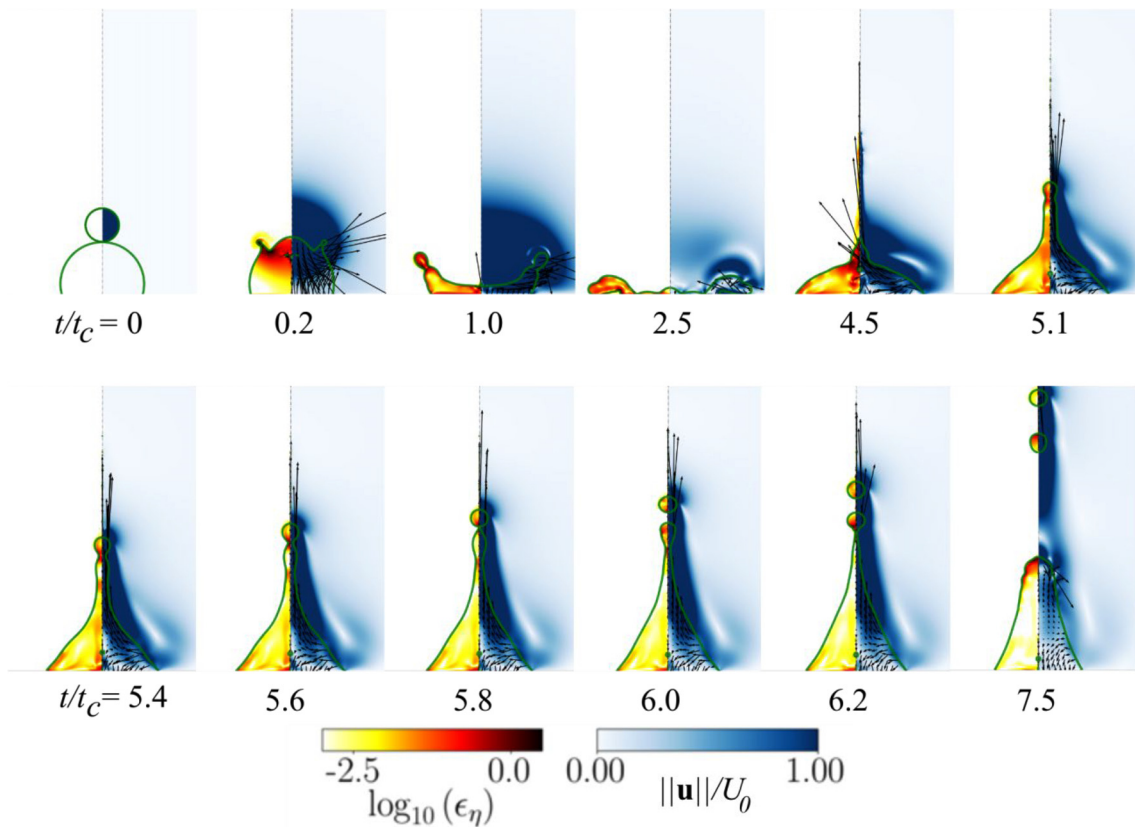

FIG. 5. (a) Numerical simulations of the reflexive separation (RS) process corresponding to the experimental case shown in Fig. 3, and (b) enlarged view near neck region ($\Delta = 3.0$, $We = 208$, $\theta_0 = 128°$, CAH $= 85°$). On the left side of numerical snapshot, the dimensionless viscous dissipation (ϵ_η) is displayed using a logarithmic scale (log10) in panel (a), dimensionless gauge pressure is displayed in panel (b), while the right side of both panels visualizes the velocity in a normalized form ($||\mathbf{u}||/U_0$).

droplet pinches off ($t/t_c = 17.9$) and forms a large spherical droplet and a conical liquid mass on the solid surface ($t/t_c = 19.2$). The conical fragment retracts and eventually forms at a smaller sessile droplet ($t/t_c = 20.0$) compared to the initial sessile droplet. It can be observed that the viscous dissipation is more prominent near the impact point and during the expansion period (until $t/t_c = 2.6$) (shown by reddish black color). The viscous dissipation is not high during the neck reduction period. It is evident from the comparison between the numerical simulation and experimental findings (Fig. 3) that the former provides a highly accurate depiction of the coalesced droplet shape and the subsequent pinch-off dynamics. Furthermore, the enlarged view near the neck region is shown in Fig. 5(b). It is seen that when the neck becomes thin ($t/t_c = 17.8$), the velocity is too high in the neck region, which removes the liquid from the neck to the top spherical liquid cap region. The velocity undergoes a transition from vertical to nearly zero and subsequently changes direction with a downward motion when traveled along the centerline ($r = 0$ line) toward the solid surface. The dashed line (red color) in Fig. 5(b), shown in the left and middle subplots, indicates the horizontal line where the flow changes direction. Following pinch-off, the lower conical liquid mass retracts and moves downward ($t/t_c = 18.0$). Furthermore, it is observed that there is a significant pressure increase near the neck region (light green region) at $t/t_c = 17.8$. At pinch-off ($t/t_c = 17.9$), high pressure is observed near

the tip of the lower conical liquid, creating resistance to the flow in the region between the pinch-off point and the horizontal dashed line.

When the droplet size ratio is decreased from 3.0 to 2.5, as seen in Fig. 6, the overall dynamics and flow patterns are similar to those observed in Fig. 5 during merged droplet expansion phase (until $t/t_c = 2.5$, Fig. 6). However, notable distinctions are observed between the two cases in the ensuing phases. Specifically, (1) a thin liquid column is formed with wide conical base ($t/t_c = 5.1$), (2) the magnitude of the velocity inside the thin liquid column is higher due to momentum conservation, (3) a neck is formed near to the tip of narrow liquid column ($t/t_c = 5.4$), which further reduces and causes pinch-off ($t/t_c = 5.8$) to form a small droplet ($t/t_c = 6.0$), and (4) another neck is formed and subsequently pinch-off occurs with a second spherical droplet (i.e., the satellite droplet) formed ($t/t_c = 6.2$). Despite the dissimilarity in droplet size predicted by the numerical simulation and the experimental observation, the pinch-off dynamics are quite similar.

Figure 7 shows the variation of normalized energies with respect to dimensionless time for reflexive separation cases, which are determined by energy budget calculations as reported in Ref. 29. The energies reported in Fig. 7 are the kinetic energy, the coalesced droplet, change in the surface energy of the coalesced droplet, and total viscous dissipation energy at the two size ratios at high We numbers (as adopted in Figs. 5 and 6). The expression for determining each energy

FIG. 6. Numerical simulations of the reflexive separation (RS) process corresponding to experimental case shown in Fig. 4 ($\Delta = 2.5$, $We = 168$, $\theta_0 = 105°$, CAH $= 88°$). On the left side of each numerical snapshot, the dimensionless viscous dissipation (ϵ_η) is displayed using a logarithmic scale (log10), while the right side visualizes the velocity in a normalized form ($||\mathbf{u}||/U_0$).
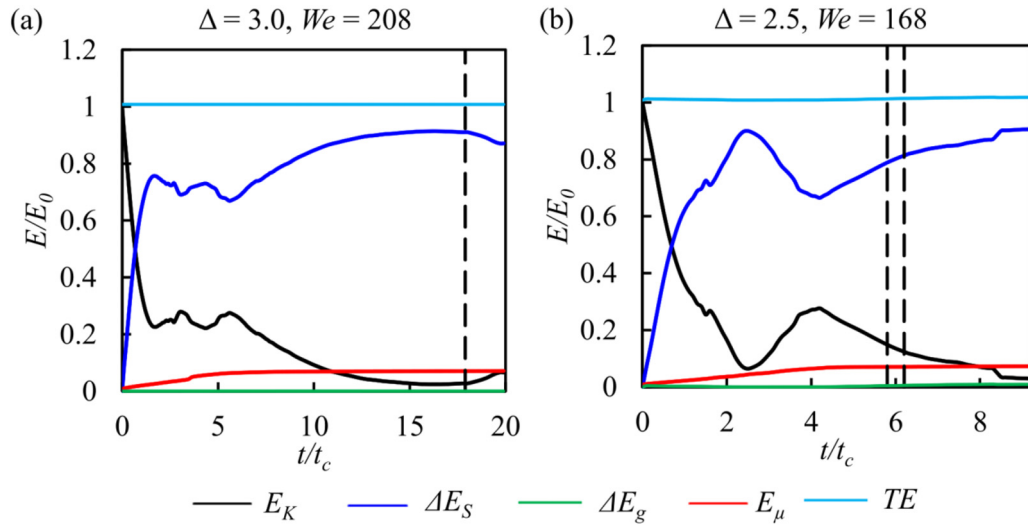
FIG. 7. Variations of different normalized energies form with non-dimensional time at (a) $\Delta = 3.0$ and $We = 208$, and (b) $\Delta = 2.5$ and $We = 168$. E denotes energy, ΔE denotes change in energy, TE denotes total energy, subscript K denotes the kinetic energy, subscript S denotes the surface energy, subscript g denotes gravitational potential energy, and subscript μ denotes total viscous dissipation. Dashed vertical lines represent pinch-off.

term is described in Appendix [see Eqs. (A2)–(A5)]. The change in potential energy is quite small ($<0.3\%$ of initial impact energy) and thus neglected. The energies are normalized with initial impact energy, E_0 [$E_0 = (1/2)(4\pi R_f^3/3)\rho_l U_0^2$]. For $\Delta = 2.5$ [Fig. 7(a)], upon impact, the kinetic energy of the merged droplet decreases with time, becomes nearly flat, then decreases slowly, and finally increases slightly after pinch-off. It can be noticed that despite maximum horizontal deform at $t/t_c = 2.6$, the kinetic energy is not the lowest. This is due to the presence of capillary waves (see Fig. 5). On the other hand, the surface energies first increase with time, remain stagnant, increase slowly, and

eventually decrease after pinch-off. The reduction in surface energy following pinch-off is expected since additional increases in surface energy are not feasible. As a result, the excess energy is converted into the kinetic energy of the pinch-off droplet (satellite droplet). At pinch-off, the normalized viscous dissipation, which amounts to approximately 7.0%, surpasses the normalized kinetic energy (i.e., 2.0%). It is also observed that the change in the gravitational potential energy is small (green color line).

The primary differences in energy distribution in Fig. 7(b) from Fig. 7(a) are as follows: (1) a minimum kinetic energy (or maximum
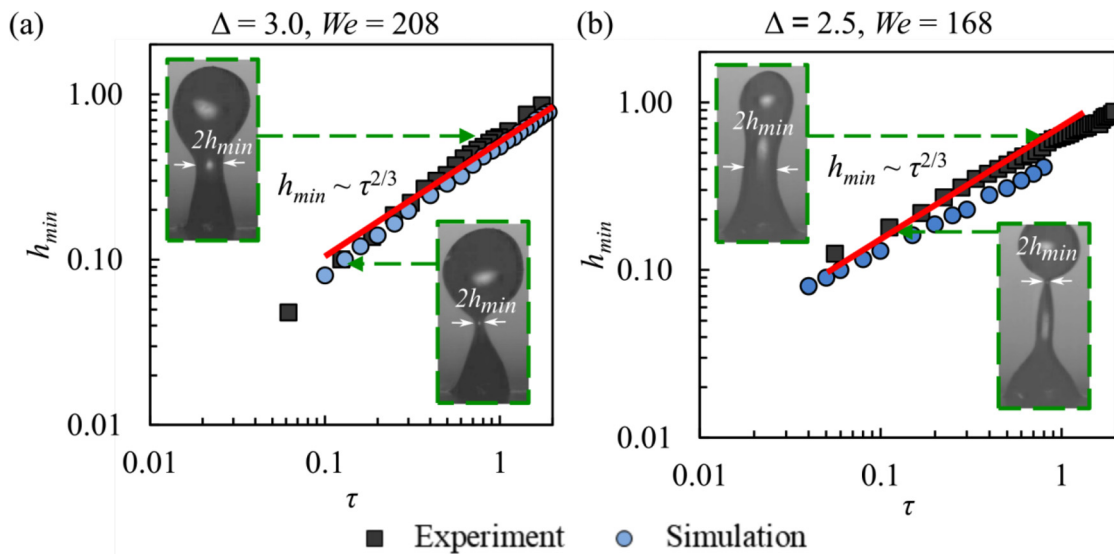

FIG. 8. The evolution of the minimum neck thickness with time τ [defined as $\tau = (t - t_p)/t_c$] at (a) $\Delta = 3.0$, and (b) $\Delta = 2.5$, with high impact We number. The minimum neck radius (h_{min}) is labeled in inset-plots in both panels. Note that the red solid line shows the trend line with a slope of 2/3.

surface energy) exists at maximum horizontal deformation [$t/t_c = 2.5$ in Fig. 7(b)], and (2) the kinetic energy decreases (or surface energy increases) after pinch-off in Fig. 7(b). It is interesting to note that the surface energy increases after pinch-off, which can be attributed to further deformation of the conical droplet mass on the solid surface (see Fig. 6, $t/t_c = 7.5$). In Fig. 7(b), it is seen that the kinetic energy (14.9% of the initial impact energy) is larger than the viscous dissipation (7.1% of the initial impact energy) at first pinch-off. The total energy (TE) remains constant, indicating a balanced energy budget.

To get insight into the pinch-off dynamics, the evolution of neck radius (h_{min}) with time τ is further analyzed. The neck is defined as the dimensionless minimum radius of the neck (see Fig. 8 insets), and time τ is defined as the time to pinch-off (t_p) minus time elapsed from the beginning of collision scaled with the inertial-capillary timescale [i.e., $\tau = (t - t_p)/t_c$]. For $\Delta = 3.0$, the neck radius decreases linearly with increasing time τ (in log–log plot). The simulation results demonstrate good agreement with the experimental data, indicating the robustness of the simulations. It has been observed that the neck radius (h_{min}) scales as $\tau^{2/3}$. Similar scaling laws have been observed in reflexive separation of head-on colliding equal-size droplets[24] and pinching-off of liquid filament.[44] When size ratio is reduced to 2.5, similar trend in neck radius with time τ is observed, namely $\tau^{2/3}$. This universal scaling of neck radius with time τ at different size ratios (Δ) could indicate that during the impact, individual droplets undergo thorough mixing and lose their distinct identities as the merged droplet is vertically stretched, eventually forming a liquid column with the subsequent formation of a neck.

To get a better understanding of the satellite formation, a regime diagram in We–Δ space is extracted from a large number of numerical simulations, as reported in Fig. 9(a). The range of We considered is 20–200, whereas Δ varies between 1 and 5. It can be seen that four different collision outcomes have been marked, namely—coalescence (C), reflexive separation without a satellite droplet (RS-0), reflexive separation with a satellite droplet (RS-1), and reflexive separation with multiple satellite droplets (RS-M). It is noticed that coalescence occurs at larger size ratio for a fixed We, whereas near unity size ratio results in breakup into multiple droplets (RS-M). The coalescence at large size ratio can be attributed to (1) the higher viscous dissipation loss (energy loss) with increasing size ratio, and (2) the enhanced ability to convert the impact kinetic energy into the surface energy of the merged droplet mass. The boundary between reflexive separation and coalescence increases, then reaches a maximum value, and decreases with increasing Δ. The various collision outcomes are marked in Fig. 9(b) at a fixed Δ (i.e., 2.0). It is seen that as Δ is decreased from 3 to 1.25 at a fixed We (i.e., 100), the collision outcomes transit from coalescence (C), reflexive separation without a satellite droplet (RS-0), reflexive separation with a satellite droplet (RS-1), and then finally breakdown of the merged droplet into multiple droplets (RS-M).

Reflexive separation (RS) typically occurs at high Weber numbers, typically ranging from $O(10)$ to $O(100)$. In RS, the impact inertia is strong enough to overcome the surface tension force. When the impact energy cannot be fully converted into surface energy, the merged droplets undergo splitting or pinching-off, resulting in RS-0. The excess energy is defined as the minimum fraction of impact kinetic energy that, when removed, prevents droplet splitting. As the Weber number increases further, the excess energy becomes more significant and can lead to the formation of satellite droplets. In this case, the
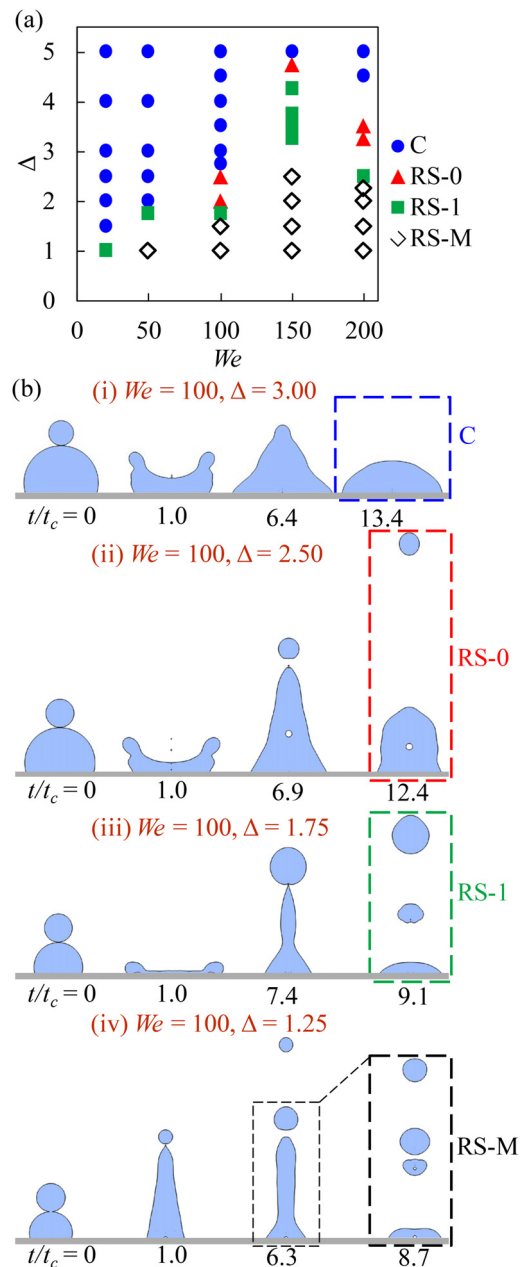

FIG. 9. (a) A regime diagram illustrating the collision outcomes in the We–Δ parameter space. (b) Different collision outcomes. Here C, RS-0, RS-1, and RS-M [corresponding to sub-panels (i)–(iv) in (b)] denote coalescence, reflexive separation without a satellite droplet, reflexive separation with a satellite droplet, and reflexive separation with multiple satellite droplets, respectively ($Oh = 0.008$, $Bo = 0.012$, $\theta_0 = 105°$, CAH $= 88°$).

excess energy is converted not only into the kinetic energy of the pinch-off droplets but also into the surface energy of the satellite droplets. Consequently, RS-1 and RS-M occur over a wider region as shown in Fig. 9(a) with increasing Weber number. It is important to note that some of the impact kinetic energy is lost due to viscous dissipation,

which is more pronounced at larger Δ. Therefore, RS is absent at lower Weber numbers and large Δ values, as indicated by the blue circle in the top left region of Fig. 9(a).

The dynamic contact angle is specified in the simulation using a fourth degree polynomial expression [see Eq. (A7) in Appendix]. Previous studies[45] have reported a sinusoidal variation of the dynamic contact angle with time for a single droplet impact on a hydrophilic surface, while the variation observed in the cases studied in this work
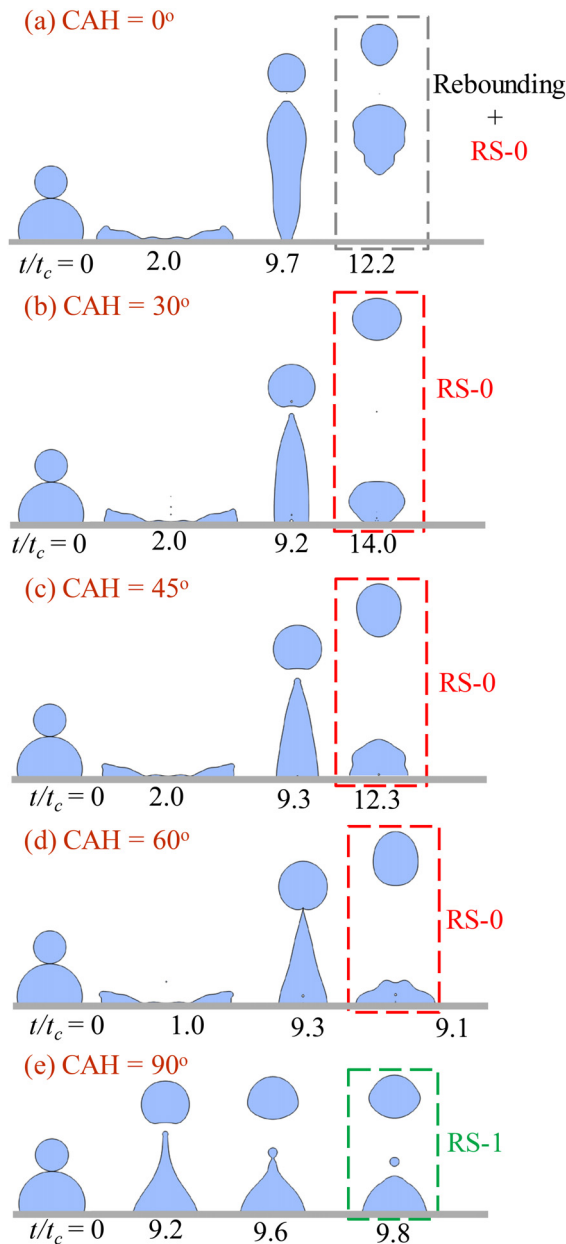
FIG. 10. Effect of contact angle hysteresis (CAH) on collision outcomes. Snapshots of simulation results at CAH values of (a) 0°, (b) 30°, (c) 45°, (d) 60°, and (e) 90°. ($We = 100$, $\Delta = 2.0$, $Oh = 0.008$, $Bo = 0.012$, $\theta_0 = 105°$.)

is different [see Fig. 12 in the Appendix]. To analyze the effect of the contact angle hysteresis (CAH), further simulations are performed at several values of CAH ranging from 0° to 90°, while the remaining parameters are fixed. The results are illustrated in Fig. 10. At CAH = 0°, the split of the merged droplet occurs, followed by the rebounding (i.e., jumping) of the sessile droplet from the solid surface. For CAH between 30°–60°, the simulation results indicate a reflexive separation without a satellite droplet (RS-0). Further increasing CAH to 90° produces a satellite droplet after reflexive separation (RS-1).

Figure 11 shows the evolution of the neck radius (h_{min}) with time τ for various CAH values ranging from 30° to 90°. The trend lines in the log–log plot appear as straight lines, showing no significant differences. This observation establishes that the neck radius (h_{min}) scales as $\tau^{2/3}$, regardless of the CAH, as long as pinch-off occurs. The identical scaling could be due to inertial dominant flow in the neck region during pinch-off (i.e., $0.1 < \tau < 1.0$).

IV. CONCLUSIONS

This study reveals the pinch-off dynamics during head-on collision of unequal-size droplets on a wetting surface via both experimental and numerical approaches, covering droplet size ratios in the range of 1.0–5.0 and impact Weber numbers up to 208. Sequential images during collision are recorded using a high-speed camera and are subsequently processed, where the experiments reveal that reflexive separation without satellite droplet formation occurs at $\Delta = 3.0$ and $We = 208$, whereas reflexive separation with satellite droplet formation occurs at $\Delta = 2.5$ and $We = 168$.

Direct numerical simulations are further carried out under conditions of the experiments, with remarkable agreements obtained with the experimental data, where the model accurately reproduces the dynamics of the pinch-off process. The velocity field reveals mechanism of the pinch-off process, where liquid moves from the neck region to top spherical cap liquid region at high velocity, further shrinking the neck and eventually leading to the pinch-off phenomenon. Energy budget calculations indicate the different energy distributions between the collisions with and without satellite droplet formation, where the surface energy decreases after pinch-off without satellite droplet formation, while an increase in surface energy is observed with the presence of a satellite droplet. Subsequently, the evolution of neck radius (h_{min}) with time τ is analyzed, with a linear
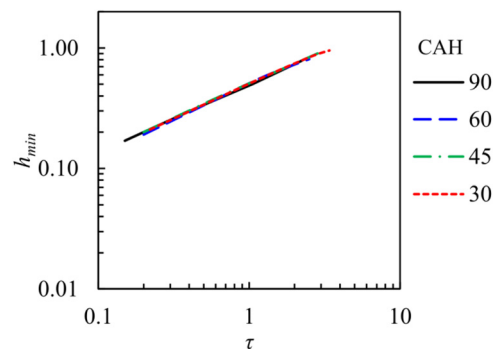
FIG. 11. The evolution of the minimum neck thickness with time τ [defined as $\tau = (t - t_p)/t_c$] at different CAH (in degree). Note that these lines shown have a slope of 2/3.

variation observed in log–log form, where the neck radius (h_{min}) scales with $\tau^{2/3}$, regardless of the droplet size ratio. A regime in We–Δ plane is reported which shows four collision outcomes, namely—coalescence (C), reflexive separation without a satellite droplet (RS-0), reflexive separation with a satellite droplet (RS-1), and reflexive separation with multiple satellite droplets (RS-M). It is shown that CAH significantly affected the collision outcomes, and thus CAH is a crucial parameter to accurately predict the collision outcomes of a falling droplet onto a sessile droplet on a solid surface.

AUTHOR DECLARATIONS
Conflict of Interest

The authors have no conflicts to disclose.

Author Contributions

Saroj Ray: Conceptualization (equal); Formal analysis (equal); Investigation (equal); Methodology (equal); Software (equal); Writing – original draft (equal); Writing – review & editing (equal). **Yu Han:** Formal analysis (supporting); Investigation (supporting); Methodology (equal). **Song Cheng:** Conceptualization (equal); Formal analysis (equal); Funding acquisition (equal); Supervision (equal); Writing – original draft (equal); Writing – review & editing (equal).

DATA AVAILABILITY

The data that support the findings of this study are available within the article.

APPENDIX: DETERMINATION OF ENERGIES AND DYNAMIC CONTACT ANGLE

1. Energy budget calculations

The energy budget utilized in this paper follows a similar approach to the one employed in Ref. 29. The absolute total energy (E_T) is calculated as the sum of the mechanical energy (E_m), surface energy (E_S), and viscous dissipation (E_μ) and can be expressed as

$$E_T = E_m + E_S + E_\mu, \tag{A1}$$

where $E_m = E_K + E_g$, E_K is the kinetic energy, and E_g is the gravitational potential energy. In this context, the energy term E_K includes both the translational kinetic energy and the energies associated with oscillation and rotation. The specific energy terms can be determined as follows:

$$E_K = \int_\Omega \frac{1}{2}\rho(\mathbf{u}\cdot\mathbf{u})d\Omega, \tag{A2}$$

$$E_g = \int_\Omega \rho \mathbf{g} z d\Omega, \tag{A3}$$

$$E_S = \int_A \gamma dA + \int_{A'} \gamma(1 - \cos\theta)dA', \tag{A4}$$

$$E_\mu = \int_0^t \left(\int_\Omega \phi d\Omega \right) dt, \tag{A5}$$

where $\mathbf{g}$, z, $d\Omega$, dA, and dA' are the acceleration due to gravity, the Z-coordinate value of the cell center, the differential volume, surface area at the liquid–gas interface, and surface area at the liquid–solid surface, respectively, and ϕ is the viscous dissipation rate (VDR). Equation (4) expresses ϕ in terms of the velocity gradients, which are determined at each grid point using backward difference of the velocity field. The velocity field information used in the calculation is obtained from the simulation performed using Basilisk C software. To determine the change in surface energy, the surface energy of the droplet is subtracted from the initial surface energy. Additionally, the gravitational potential energy of the droplet is taken as zero at its lowest center of mass location. Thus, Eq. (A1) can be rewritten as

$$TE = E_K + \Delta E_g + \Delta E_S + E_\mu, \tag{A6}$$

where TE represents the total energy, while ΔE denotes the change in the energy. All the energy terms in Eq. (A6) are plotted in Fig. 7.

2. Contact angle

The variation of the dynamic contact angle with time can be determined by measuring the contact angle of each image in the experimental image sequence. The method to measure the contact angle is reported in Ref. 32. Figure 12 shows the variation of the normalized contact angle and the scaled time. The normalized contact angle is defined as $\hat{\theta} = \frac{\theta - \theta_0}{\theta_{max} - \theta_{min}}$, where θ is the contact angle and subscripts 0, min, and max denote initial, minimum, and maximum, respectively. It can be noticed that the denominator of $\hat{\theta}$ is the contact angle hysteresis (CAH $= \theta_{max} - \theta_{min}$). The scaled time is defined as $\hat{t} = (1 + 1/\Delta^2)(t/t_c)$. For single droplet impact $\Delta = \infty$, thus $\hat{t} = t/t_c$. It is seen from Fig. 12 that the normalized contact angle exhibits a sinusoidal pattern when a single droplet
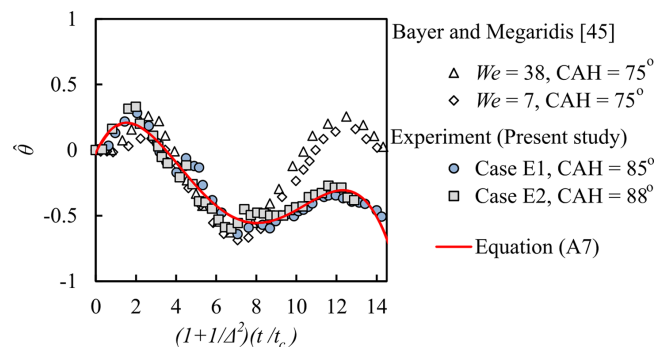
FIG. 12. The variation of the normalized contact angle with scaled time. The experimental data are taken from Bayer and Megaridis[45] and the present study.

impacts a hydrophobic surface.[45] A similar trend is observed in this study for the collision of unequal-sized droplets on a hydrophobic surface, but only for $\hat{t} < 9.0$. Beyond $\hat{t} > 9.0$, the normalized contact angle values are lower compared to the single droplet impact scenario. In other words, the second peak height is lower. It is observed that the variation of the normalized contact angle is small for $\hat{t} > 10.0$. Furthermore, a fourth degree polynomial is fitted to obtain a relationship between the normalized contact angle and scaled time and is expressed as

$$\hat{\theta} = a_1\hat{t}^4 + a_2\hat{t}^3 + a_3\hat{t}^2 + a_4\hat{t} + a_5, \qquad (A7)$$

where a_1–a_5 are constant, whose values have been determined as $a_1 = -5.516 \times 10^{-4}$, $a_2 = 1.615 \times 10^{-2}$, $a_3 = -1.447 \times 10^{-1}$, $a_4 = 3.407 \times 10^{-1}$, and $a_5 = -3.382 \times 10^{-2}$. To avoid extrapolation error, Eq. (A7) is used until $\hat{t} = 14.0$. For $\hat{t} > 14.0$, the normalized contact angle is fixed at -0.506, which corresponds to the $\hat{\theta}$ value at $\hat{t} = 14.0$. The explicit expression (A7) provides a convenient ways to specify the dynamic contact angle with time, where parameters such as θ_0, Δ, and CAH can be changed easily. Thus, Eq. (A7) is used to specify the dynamic contact angles in simulations for this study. A good agreement of the simulation results with the experiment (e.g., see Fig. 8) suggests that the present approach is quite accurate.

REFERENCES

[1]J. Mostaghimi, S. Chandra, R. Ghafouri-Azar, and A. Dolatabadi, "Modeling thermal spray coating processes: A powerful tool in design and optimization," Surf. Coat. Technol. **163–164**, 1–11 (2003).

[2]A. Moridi, S. M. Hassani-Gangaraj, M. Guagliano, and M. Dao, "Cold spray coating: Review of material systems and future perspectives," Surf. Eng. **30**(6), 369–395 (2014).

[3]V. Bergeron, D. Bonn, J. Y. Martin, and L. Vovelle, "Controlling droplet deposition with polymer additives," Nature **405**, 772 (2000).

[4]R. J. Gilliom, J. E. Barbash, C. G. Crawford, P. A. Hamilton, J. D. Martin, N. Nakagaki, L. H. Nowell, J. C. Scott, P. E. Stackelberg, and G. P. Thelin, Pesticides in the nation's streams and ground water 1992–2001, Circular Report No. 1291, The Quality of Our Nation's Waters, 184 (U.S. Geological Survey, 2006), p.184.

[5]C. K. Law, *Combustion Physics* (Cambridge University Press, 2010).

[6]J. Adam, N. Lindblad, and C. Hendricks, "The collision, coalescence, and disruption of water droplets," J. Appl. Phys. **39**(11), 5173 (1968).

[7]N. Ashgriz and J. Poo, "Coalescence and separation in binary collisions of liquid drops," J. Fluid Mech. **221**, 183 (1990).

[8]Y. J. Jiang, A. Umemura, and C. K. Law, "An experimental investigation on the collision behavior of hydrocarbon droplets," J. Fluid Mech. **234**, 171 (1992).

[9]J. Qian and C. K. Law, "Regimes of coalescence and separation in droplet collision," J. Fluid Mech. **331**, 59 (1997).

[10]K. L. Pan, P. C. Chou, and Y. J. Tseng, "Binary droplet collision at high Weber number," Phys. Rev. E **80**(3), 036301 (2009).

[11]C. Tang, P. Zhang, and C. K. Law, "Bouncing, coalescence, and separation in head-on collision of unequal-size droplets," Phys. Fluids **24**(2), 022101 (2012).

[12]M. Orme, "Experiments on droplet collisions, bounce, coalescence and disruption," Prog. Energy Combust. Sci. **23**(1), 65–79 (1997).

[13]J. P. Estrade, H. Carentz, G. Lavergne, and Y. Biscos, "Experimental investigation of dynamic binary collision of ethanol droplets–a model for droplet coalescence and bouncing," Int. J. Heat Fluid Flow **20**(5), 486–491 (1999).

[14]G. Brenn, D. Valkovska, and K. D. Danov, "The formation of satellite droplets by unstable binary drop collisions," Phys. Fluids **13**(9), 2463–2477 (2001).

[15]G. Brenn and V. Kolobaric, "Satellite droplet formation by unstable binary drop collisions," Phys. Fluids **18**(8), 087101 (2006).

[16]H. Deka, G. Biswas, S. Chakraborty, and A. Dalal, "Coalescence dynamics of unequal sized drops," Phys. Fluids **31**(1), 012105 (2019).

[17]G. S. Chaitanya, K. C. Sahu, and G. Biswas, "A study of two unequal-sized droplets undergoing oblique collision," Phys. Fluids **33**(2), 022110 (2021).

[18]P. R. Brazier-Smith, S. G. Jennings, and J. Latham, "The interaction of falling water drops: Coalescence," Proc. R. Soc. A: Math. Phys. Eng. **326**(1566), 393–408 (1972).

[19]S. T. Thoroddsen and K. Takehara, "The coalescence cascade of a drop," Phys. Fluids **12**(6), 1265–1267 (2000).

[20]F. Blanchette and T. P. Bigioni, "Partial coalescence of drops at liquid interfaces," Nat. Phys. **2**(4), 254–257 (2006).

[21]F. H. ZhangE, Q. Li, and S. T. Thoroddsen, "Satellite formation during coalescence of unequal size drops," Phys. Rev. Lett. **102**(10), 104502 (2009).

[22]K. Willis and M. Orme, "Binary droplet collisions in a vacuum environment: An experimental investigation of the role of viscosity," Exp. Fluids **34**(1), 28–41 (2003).

[23]C. Planchette, E. Lorenceau, and G. Brenn, "The onset of fragmentation in binary liquid drop collisions," J. Fluid Mech. **702**, 5–25 (2012).

[24]K. L. Huang, K. L. Pan, and C. Josserand, "Pinching dynamics and satellite droplet formation in symmetrical droplet collisions," Phys. Rev. Lett. **123**(23), 234502 (2019).

[25]H. Deka, G. Biswas, and B. J. Bora, "Head-on collision of dissimilar viscosity drops," Langmuir **39**, 8130–8140 (2023).

[26]F. C. Wang, J. T. Feng, and Y. P. Zhao, "The head-on colliding process of binary liquid droplets at low velocity: High-speed photography experiments and modeling," J. Colloid Interface Sci. **326**(1), 196 (2008).

[27]J. Wakefield, C. F. Tilger, and M. A. Oehlschlaeger, "The interaction of falling and sessile drops on a hydrophobic surface," Exp. Therm. Fluid Sci. **79**, 36 (2016).

[28]M. Damak and K. Varanasi, "Expansion and retraction dynamics in drop-on-drop impacts on nonwetting surfaces," Phys. Rev. Fluids **3**(9), 093602 (2018).

[29]O. Ramírez-Soto, V. Sanjay, D. Lohse, J. T. Pham, and D. Vollmer, "Lifting a sessile oil drop from a superamphiphobic surface with an impacting one," Sci. Adv. **6**(34), eaba4330 (2020).

[30]M. Kumar, R. Bhardwaj, and K. C. Sahu, "Coalescence dynamics of a droplet on a sessile droplet," Phys. Fluids **32**(1), 012104 (2020).

[31]M. Abouelsoud and B. Bai, "Bouncing and coalescence dynamics during the impact of a falling drop with a sessile drop on different solid surfaces," Phys. Fluids **33**(6), 063309 (2021).

[32]S. Ray, Y. Chi, P. Zhang, and S. Cheng, "Head-on collision of unequal-size droplets on a wetting surface," Phys. Fluids **35**, 022114 (2023).

[33]C. He and P. Zhang, "Nonaxisymmetric flow characteristics in head-on collision of spinning droplets," Phys. Rev. Fluids **5**(11), 113601 (2020).

[34]C. He, Z. He, and P. Zhang, "Oblique bouncing of a droplet from a non-slip boundary: Computational realization and application of self-spin droplets," Int. J. Multiphase Flow **167**, 104548 (2023).

[35]P. K. Kirar, S. D. Pokale, K. C. Sahu, B. Ray, and G. Biswas, "Influence of the interaction of capillary waves on the dynamics of two drops falling side-by-side on a liquid pool," Phys. Fluids **34**(11), 112114 (2022).

[36]L. F. Alventosa, R. Cimpeanu, and D. M. Harris, "Inertio-capillary rebound of a droplet impacting a fluid bath," J. Fluid Mech. **958**, A24 (2023).

[37]Y. Couder, S. Protiere, E. Fort, and A. Boudaoud, "Walking and orbiting droplets," Nature **437**(7056), 208–208 (2005).

[38]J. W. Bush and A. U. Oza, "Hydrodynamic quantum analogs," Rep. Prog. Phys. **84**(1), 017001 (2020).

[39]J. U. Brackbill, D. B. Kothe, and C. Zemach, "A continuum method for modeling surface tension," J. Comput. Phys. **100**(2), 335–354 (1992).

[40]P. Popinet, see http://basilisk.fr/ for "The basilisk code."

[41]C. He, X. Xia, and P. Zhang, "Non-monotonic viscous dissipation of bouncing droplets undergoing off-center collision," Phys. Fluids **31**(5), 052004 (2019).

[42]J. Sakakeeny and Y. Ling, "Natural oscillations of a sessile drop on flat surfaces with mobile contact lines," Phys. Rev. Fluids **5**(12), 123604 (2020).

[43]S. Afkhami and M. Bussmann, "Height functions for applying contact angles to 3d VOF simulations," Int. J. Numer. Methods Fluids **61**, 827–847 (2009).

[44]Y. J. Chen and P. H. Steen, "Dynamics of inviscid capillary breakup: Collapse and pinchoff of a film bridge," J. Fluid Mech. **341**, 245–267 (1997).

[45]I. S. Bayer and C. M. Megaridis, "Contact angle dynamics in droplets impacting on flat surfaces with different wetting characteristics," J. Fluid Mech. **558**, 415–449 (2006).

16 October 2024 06:30:38